

Kinetically Controlled Epitaxial Growth of Fe₃GeTe₂ van der Waals Ferromagnetic Films

Wenyi Zhou, Alexander J. Bishop, Menglin Zhu, Igor Lyalin, Robert Walko, Jay A. Gupta, Jinwoo Hwang, and Roland K. Kawakami*

Cite This: <https://doi.org/10.1021/acsaelm.2c00185>

Read Online

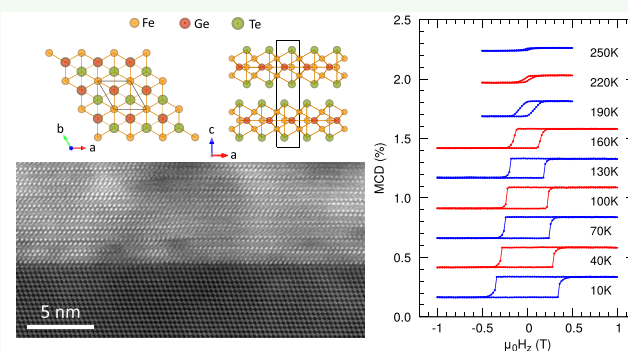
ACCESS |

Metrics & More

Article Recommendations

ABSTRACT: We demonstrate that kinetics play an important role in the epitaxial growth of Fe₃GeTe₂ (FGT) van der Waals (vdW) ferromagnetic films by molecular beam epitaxy. By varying the deposition rate, we control the formation or suppression of an initial tellurium-deficient non-van-der-Waals phase (Fe₃Ge₂) prior to realizing epitaxial growth of the vdW FGT phase. Using cross-sectional scanning transmission electron microscopy and scanning tunneling microscopy, we optimize the FGT films to have atomically smooth surfaces and abrupt interfaces with the Ge(111) substrate. The magnetic properties of our high quality material are confirmed through magneto-optic, magnetotransport, and spin-polarized STM studies. Importantly, this demonstrates how the interplay of energetics and kinetics can help tune the re-evaporation rate of chalcogen atoms and interdiffusion from the underlayer, which paves the way for future studies of van der Waals epitaxy.

KEYWORDS: 2D materials, van der Waals magnet, ferromagnetism, molecular beam epitaxy, growth kinetics, transmission electron microscopy, magnetic circular dichroism, spin-polarized scanning tunneling microscopy



INTRODUCTION

There is tremendous interest in ultrathin van der Waals magnets because of the unprecedented tunability of magnetic properties via strain,^{1–3} electrostatic gating,^{4,5} and incorporation into heterostructures.^{6–9} Fe₃GeTe₂ (FGT) (Figure 1a) is one of the most well-studied vdW magnets because of its strong perpendicular magnetic anisotropy (PMA), relatively high Curie temperature (T_C) ranging from ~200 K to above room temperature,^{10–15} and observation of novel phenomena such as spin–orbit torque switching^{14–17} and skyrmion spin textures.^{18–20}

While many efforts have focused on small flakes exfoliated from bulk crystals, the epitaxial growth of thin films and heterostructures by methods such as molecular beam epitaxy (MBE) provide unique opportunities. This includes stabilizing materials far from equilibrium that cannot be realized in bulk crystal form (e.g., vdW MnBi₂Se₄²¹), performing atomic-scale manipulation of interface structure and material properties, and enabling scaling up to large areas for electronic and magnetic applications.

To date, there have been several reports of epitaxial growth of FGT and related materials by MBE (e.g., FGT films on Al₂O₃(0001),²² GaAs(111),²² Ge(111),²³ and Bi₂Te₃(0001);^{13,17,24} Fe₃GeTe₂ on Al₂O₃(0001)²⁵). However,

critical issues of the growth process, such as the relative importance of thermodynamic equilibrium (energetics) and growth/reaction rates (kinetics), remain largely unexplored. Understanding these issues are important for improving the material quality as it relates to important properties of thin films and heterostructures including interdiffusion and defect formation.

In this work, we demonstrate that kinetics play an important role in the epitaxial growth of FGT films by MBE. For FGT grown on Ge(111), we find that growth rate is a critical parameter that determines whether FGT grows directly on Ge(111) with an atomically abrupt interface or whether a Te-deficient non-vdW Fe₃Ge₂ alloy forms at the interface. Contrary to expectations for reactive MBE growth,^{26,27} our studies show that the Fe₃Ge₂ alloy forms at lower growth rates, while the abrupt FGT/Ge(111) interface is obtained for higher growth rates. This behavior suggests that energetic consid-

Special Issue: 2D Magnetism - Materials, Devices, and Applications

Received: February 8, 2022

Accepted: March 29, 2022

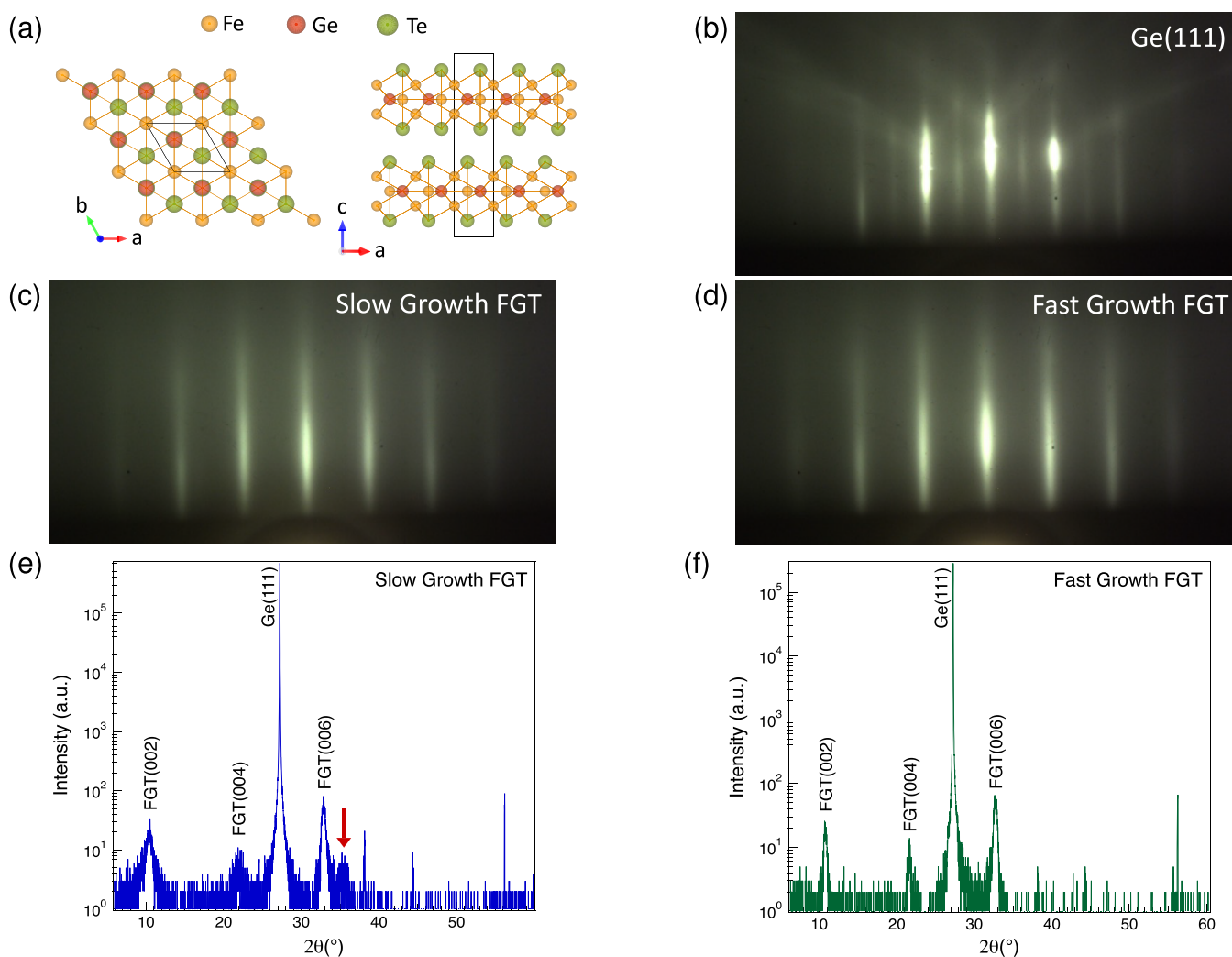


Figure 1. MBE-grown Fe_3GeTe_2 (FGT) films on Ge(111) at different growth rates. (a) Atomic lattice of FGT, where the crystal unit cell is outlined. (b) RHEED pattern of Ge(111) substrate. (c) RHEED pattern for 40 nm FGT grown at 0.06 \AA/s (slow growth FGT). (d) RHEED pattern for 20 nm FGT grown at 0.12 \AA/s (fast growth FGT). (e) $\theta - 2\theta$ X-ray diffraction scan of slow growth FGT (40 nm). The red arrow indicates the presence of an unexpected additional peak. (f) $\theta - 2\theta$ X-ray diffraction scan of fast growth FGT (20 nm), which does not exhibit the additional peak.

erations favor the formation of non-vdW Fe–Ge alloys, while the growth kinetics can favor the stabilization of pure FGT. The high quality of the pure FGT films is corroborated by their excellent magnetic properties, where $\sim 20 \text{ nm}$ FGT films on Ge(111) exhibit properties similar to bulk FGT, including perpendicular magnetic anisotropy with square hysteresis loops and a T_C of $\sim 250 \text{ K}$. These results demonstrate that the interplay of energetics and kinetics can help tune the re-evaporation rate of chalcogen atoms and interdiffusion from the underlayer to facilitate the development of high quality vdW epitaxial films.

EXPERIMENTAL SECTION

The FGT films were deposited in a Veeco 930 MBE system with base pressure of $2 \times 10^{-10} \text{ Torr}$. The Ge(111) substrates (MTI Corporation) were prepared by sonication in acetone and isopropyl alcohol for 5 min each before being inserted into the MBE chamber. After degassing at $800 \text{ }^\circ\text{C}$ for 12 min, the Ge substrates were cooled to $325 \text{ }^\circ\text{C}$ for growth of the FGT films. For synthesis, the films were grown by codepositing Fe (99.99%, Alfa Aesar), Ge (99.9999%, Alfa Aesar), and Te (99.9999%, United Mineral Corp.) with an atomic flux ratio of 3:1:20, as measured by a beam flux monitor (BFM) and

calibrated by X-ray reflectivity (XRR) of elemental films. Prior to growth, the substrate was exposed to the Te flux for 5 min.

We employed a wide range of characterizations including *in situ* reflection high energy electron diffraction (RHEED) and *ex situ* X-ray diffraction to probe the surface and bulk crystal structure, respectively. The atomic-scale structure was investigated by scanning tunneling microscopy (STM) and cross-sectional scanning transmission electron microscopy (STEM) with elemental analysis (i.e., energy dispersive X-ray spectroscopy (EDX)). Magnetic properties were investigated by anomalous Hall effect (AHE), optical magnetic circular dichroism (MCD), and spin-polarized STM.

For cross-sectional STEM imaging, specimens were prepared using conventional focused ion beam lift-out technique with Helios NanoLab 600. Argon ion milling under 900 and 500 eV was used subsequently to clean the surface amorphous layer and minimize subsurface damage. High-angle annular dark field (HAADF) STEM images and EDX maps were collected using a probe-aberration corrected Thermo Fisher Scientific Themis Z S/TEM operated at 300 kV, 20 mrad convergence semiangle.

For STM measurements, samples mounted on flag-style sample holders were transferred from the MBE chamber to the STM using a UHV suitcase to keep the sample under vacuum during the entire sample transfer. The STM measurements were performed in a Cretec LT-STM/AFM system with the sample held at a temperature

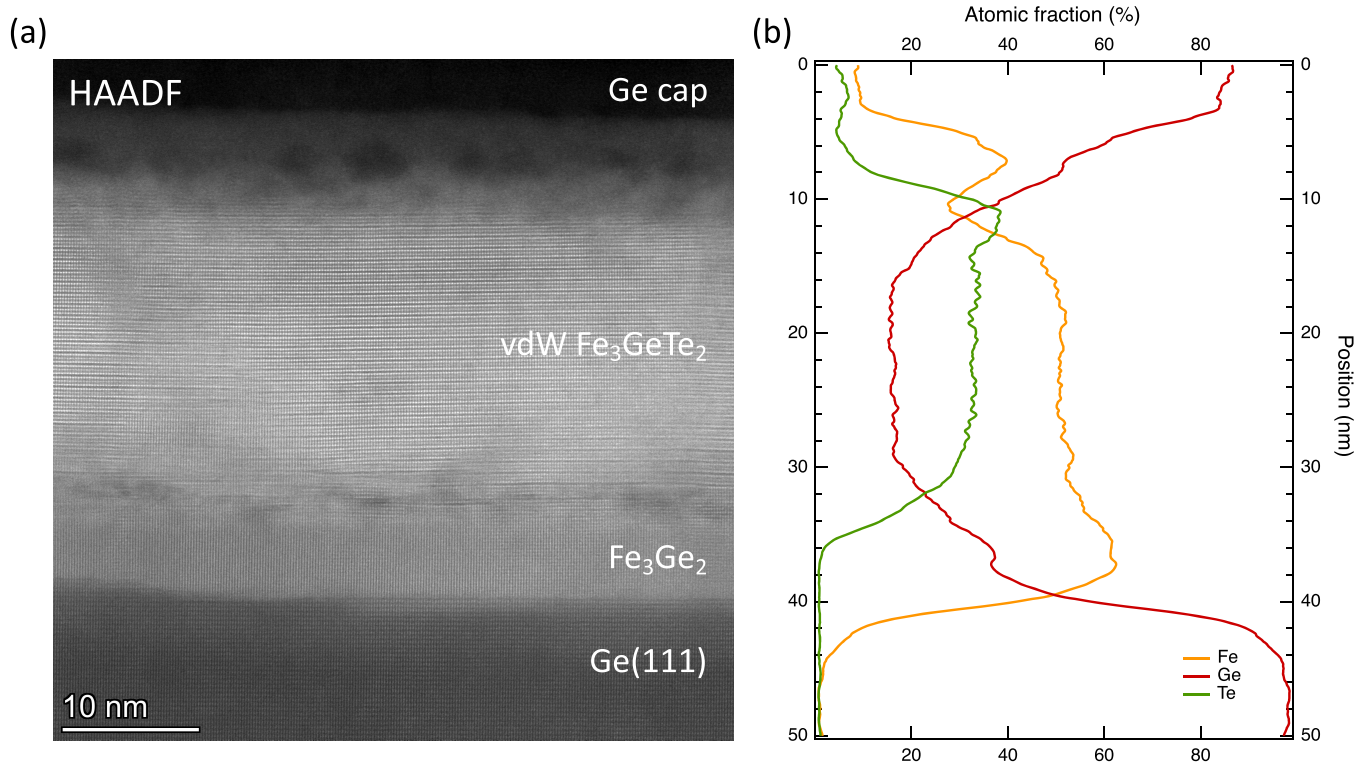


Figure 2. Scanning transmission electron microscopy (STEM) of slow growth FGT on Ge(111). (a) Cross-sectional STEM image of slow growth FGT (0.06 Å/s). (b) Energy-dispersive X-ray spectroscopy (EDX) of slow growth FGT as a function of depth, showing Te deficiency during the initial growth.

of 5 K. Spin-polarized STM measurements utilized a Cr tip and an out-of-plane magnetic field.

We performed AHE and MCD measurements in an Oxford Spectromag magneto-optical cryostat. To obtain out-of-plane hysteresis loops, we applied a magnetic field perpendicular to the surface of the sample. The AHE measurements were performed using lock-in detection at 987 Hz and an excitation current of 100 μ A (rms). For MCD measurements, we utilized a 100 μ W, 532 nm laser beam focused to a spot size of \sim 150 μ m. The helicity of the incident beam was modulated at 50 kHz by a photoelastic modulator and the MCD of the reflectivity was measured using an amplified Si photodiode and lock-in detection.

RESULTS AND DISCUSSION

Growth and Structural Characterization. In studying the epitaxial growth of FGT on Ge(111), we observe a fascinating dependence of the materials quality on the growth rate. To illustrate, we employ two representative growth rates, namely, a “slow growth” rate of \sim 0.06 Å/s and a “fast growth” rate of \sim 0.12 Å/s, where the growth rate is increased by raising the atomic fluxes of Fe, Ge, and Te while maintaining a 3:1:20 ratio. Starting from streaky RHEED patterns of the Ge(111) substrate (Figure 1b), in both cases, we observe streaky RHEED throughout the growth as shown in Figure 1c and d. In addition, the streak spacing matches the FGT in-plane lattice constant in both cases. However, the X-ray diffraction (XRD) shows different features for slow growth and fast growth, even though their RHEED patterns are very similar. For slow growth FGT in Figure 1e, it can be seen that the $\theta - 2\theta$ XRD scan has an unexpected extra peak of unknown origin (red arrow) beside the FGT(006) peak. But for fast growth FGT in Figure 1f, the extra peak in the XRD scan no longer

exists. This indicates a pure phase FGT film for fast growth and a mixed phase FGT film for slow growth.

To better understand this phenomenon, we perform cross-sectional STEM for atomic-scale characterization of the structure and chemical composition. For the slow growth FGT (Figure 2a), we observe a non-vdW phase at the initial growth on the Ge substrate. But good vdW layers subsequently grow on top of this initial non-vdW phase. The vdW layers are clearly visible in the STEM image by the bright horizontal lines. The chemical composition shown in the EDX scan (Figure 2b) provides some key insights. In the top part of the film, the stoichiometry of Fe, Ge, and Te is 3.13:1.00:2.03 (averaged in between position 20 and 26 nm) indicating the formation of the vdW magnet Fe_3GeTe_2 . In the bottom part of the film, the Te atomic fraction goes to zero and the Fe and Ge atoms have a ratio of \sim 1.56 (averaged in between position 36 and 39 nm), which suggests the alloy Fe_3Ge_2 . This conclusion is further supported by the extra peak in the XRD corresponding to a lattice spacing of \sim 5.04 Å, which is close to the lattice spacing of 5.010 Å^{28,29} for Fe_3Ge_2 along the [001] direction (hexagonal c-plane). In addition, Fe_3Ge_2 has an in-plane lattice constant of $a = b = 3.998$ Å^{28,29} which is very similar to that of FGT ($a = b = 3.991$ Å^{23,30,31}). This explains why it is hard to tell the difference between FGT and Fe_3Ge_2 in RHEED during growth. Thus, the EDX, XRD, and RHEED provide strong evidence that the non-vdW interfacial phase is (001)-oriented Fe_3Ge_2 .

The fast growth FGT on Ge(111) exhibits quite different behavior. As shown in Figure 3a, cross-sectional STEM imaging reveals that vdW FGT layers form immediately at the start of growth. Again, the vdW layers are clearly visible in the TEM by the bright horizontal lines. Moreover, a close look

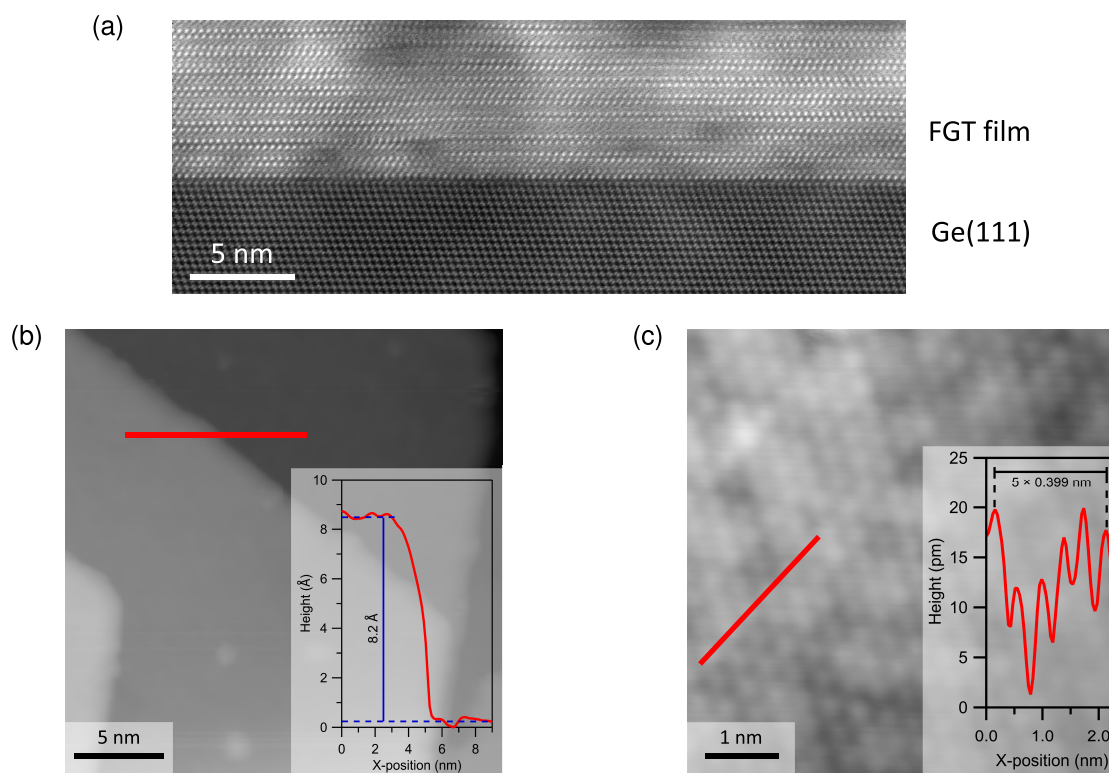


Figure 3. Atomic scale structural characterization of fast growth FGT on Ge(111). (a) Cross-sectional STEM image of fast growth FGT showing atomically abrupt interfaces between the van der Waals FGT and the Ge substrate. (b) Surface morphology of fast growth FGT measured by STM. Inset: Height profile line cut across a step-edge indicated by the solid red line (tunneling conditions: sample bias $V = -154$ mV, $I = 0.22$ nA). (c) Atomically resolved imaging of Te terminated FGT measured by STM. Inset: Line cut profile indicated by the solid red line with a periodicity of 3.99 Å (tunneling conditions: sample bias $V = 100$ mV, $I = 0.15$ nA).

at the interface shows an atomically sharp transition between the Ge substrate and the FGT film, which indicates that the vdW FGT layers form immediately at the interface. This is a great improvement over the slow growth FGT (Figure 2), which has a transition layer of Fe_3Ge_2 in between the Ge substrate and the FGT film. However, there is still room for improvement, as some defects are visible.

STM measurements on a fast growth FGT sample, shown in Figure 3b and c, also support the high quality of films grown by this method. Figure 3b shows large atomically flat terraces with a line cut across a step edge. The height profile of the line cut, displayed in the inset, indicates that the two terraces differ in height by 8.2 Å, which is in good agreement with the height of a single vdW layer of FGT. Atomic resolution imaging (Figure 3c) reveals a well ordered hexagonal lattice with an in-plane lattice constant of 3.99 Å, consistent with the topmost Te layer of an FGT vdW layer. These results indicate that the growth method established here facilitates good layer-by-layer growth with consistent Te termination.

Magnetic Properties. For the fast growth FGT/Ge(111) samples, we investigate the out-of-plane hysteresis loops by measuring the anomalous Hall effect (AHE), reflection magnetic circular dichroism (MCD), and spin-polarized STM. Figure 4a and b shows out-of-plane hysteresis loops of a 20 nm fast growth FGT film measured by AHE and MCD, respectively, at 2 K. The AHE measurement exhibits a square hysteresis loop and a coercivity of ~ 0.379 T, similar to values reported in the literature. Similarly, the hysteresis loop measured by MCD exhibits virtually identical characteristics as the AHE hysteresis loop measured in the same cryostat. The

temperature dependence of the MCD hysteresis loops is shown in Figure 4c. From 10 to 130 K, the hysteresis loops remain square and the coercivity reduces from 0.355 to 0.199 T. From 160 to 250 K, the magnetization reversal becomes more gradual and the coercivity continues to decrease. The magnitude of the MCD signal reduces to nearly zero at 250 K, leading to an estimated T_C of ~ 250 K. This is slightly higher than the bulk T_C of 230 K,^{10,30,32} but the origin of the enhancement is unclear and warrants further study. These magnetic properties reflect the high quality of the epitaxial films.

Spin-polarized STM measurements³³ are performed using a Cr tip and sweeping the out-of-plane magnetic field. The magnetic contrast is observed in the dI/dV signal at a sample bias of 100 mV and a tip current of 0.15 nA. As shown in Figure 4d, the dI/dV signal shows sharp switching indicated by black arrows at 0.42 T for the positive field ramp (blue) and at -0.48 T for the negative field ramp (red). Unlike the MCD measurement which averages the magnetization within the ~ 150 μm laser spot, the STM measurement is local at the atomic scale. This explains why MCD hysteresis loops are more uniform, while the STM hysteresis loop has switchings that occur at different field magnitudes. The latter reflects the stochastic nature of magnetization reversal. Future studies are planned to capture images of the magnetic domain structure during a magnetization reversal.

DISCUSSION

We now consider why growth rate is such an important factor in determining the material quality during the initial growth.

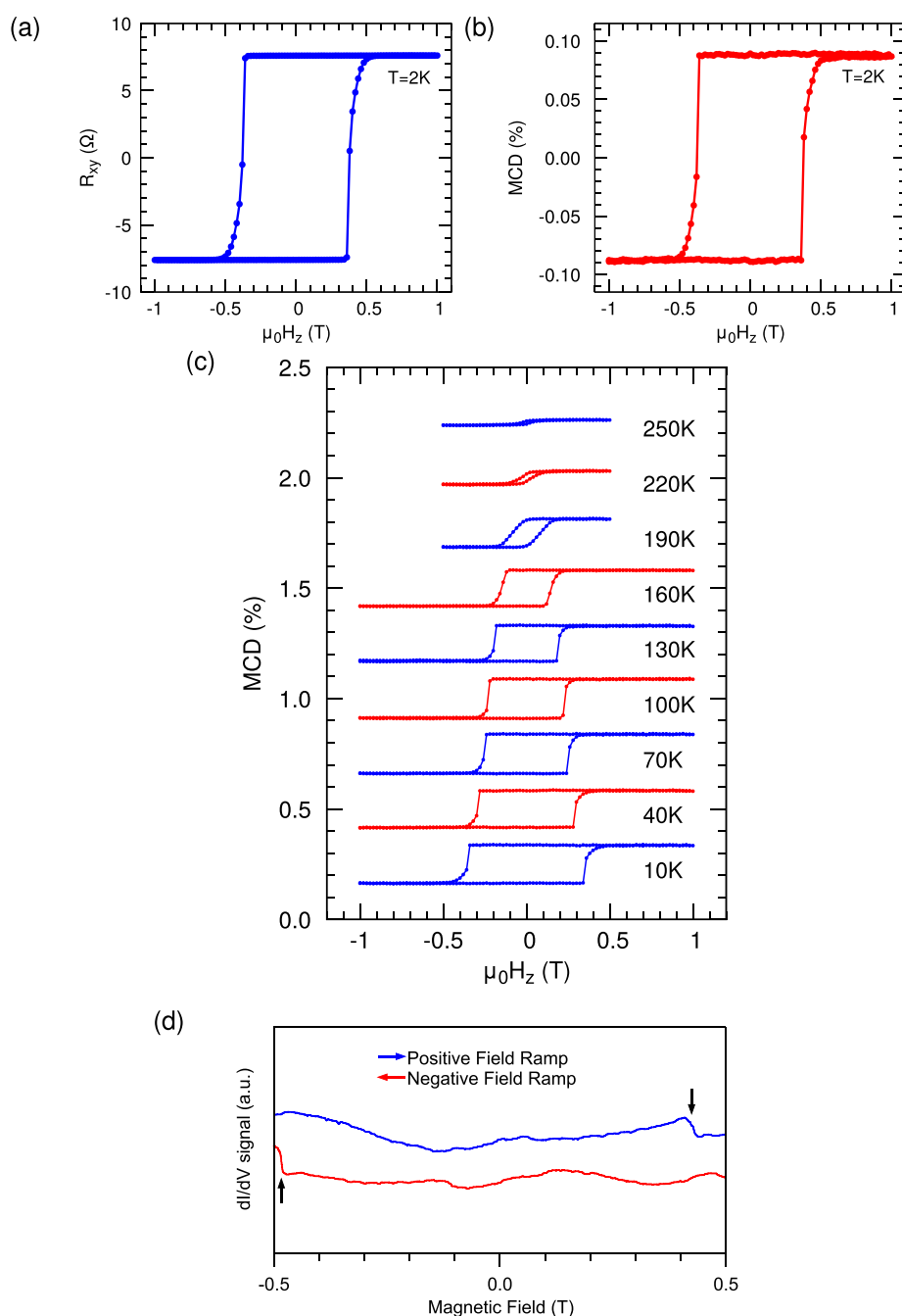


Figure 4. Out-of-plane magnetic hysteresis loops of fast growth FGT. (a) Anomalous Hall effect measurement at 2 K. (b) Magnetic circular dichroism (MCD) measurement at 2 K. (c) MCD for a series of temperatures, showing a T_C of ~ 250 K. Curves have been vertically offset. (d) Spin-polarized scanning tunneling microscopy measurement at 5 K. The data has been filtered for noise reduction. Curves have been offset for clarity.

The fact that the synthesis depends strongly on growth rate implies the importance of kinetics, or the rate of material processes (e.g., interdiffusion, chemical reaction, atomic diffusion on surfaces, re-evaporation, etc.). The complementary factor that is significant for material synthesis is the thermodynamic equilibrium phase which minimizes the free energy. The balance between energetics and kinetics can be controlled by the growth rate, where slower growth rates favor the equilibrium phase and faster growth rates can produce materials further away from equilibrium based on kinetic considerations.

In applying these concepts to our case, we first point out that the growth conditions with a 10 \times overpressure of Te (i.e., Fe: Ge: Te beam flux ratio of 3:1:20 for Fe_3GeTe_2 with a stoichiometry of 3:1:2) is a typical condition for reactive MBE, where the volatile species (Te) reacts with the other elements to form the desired material with proper stoichiometry due to re-evaporation of excess Te. In reactive MBE, when the film has a deficiency of the volatile species, typical solutions are to increase its beam flux or reduce the growth rate. This allows more time for the reaction to occur and can increase the incorporation of the volatile species into the material. But our FGT growth appears to behave in an opposite way, so we

would not consider this process as traditional reactive MBE. Since slower growth favors the equilibrium phase while faster growth is further from equilibrium, this suggests that a Fe_3Ge_2 surface is more thermodynamically stable than the FGT surface within a partial pressure of 10^{-8} to 10^{-7} Torr of Te and at 325 °C during the initial stages of growth. In other words, energetics favor formation of Fe_3Ge_2 . Thus, in order to stabilize the FGT phase that we want, we must consider the rate kinetics associated with the growth. In comparing the chemical composition of Fe_3Ge_2 with Fe_3GeTe_2 , the Fe_3Ge_2 has a higher relative content of Ge (Ge: Fe = 2:3 for Fe_3Ge_2 vs 1:3 for FGT) and an absence of Te. The absence of Te in Fe_3Ge_2 is achieved by the out-diffusion of Te from the film into vacuum. For the increased Ge: Fe ratio (2:3) relative the beam flux ratio (1:3), either the sticking coefficient of the Fe must become lower than that of Ge or the excess Ge is supplied by the substrate. Since the cell temperature for Fe of ~ 1300 °C is much higher than the substrate temperature of 325 °C, this argues against a reduced sticking coefficient of Fe and strongly supports the scenario that the excess Ge is supplied via interdiffusion from the substrate. This is also supported by the fact that the growth eventually converts to a vdW FGT phase. Thus, to stabilize the FGT phase that we want (and avoid Fe_3Ge_2), the growth rate must be sufficiently high to outpace the out-diffusion of Te from the film surface and the interdiffusion of Ge into the film. One would expect the required minimum growth rate to be temperature dependent. Lower temperatures have slower diffusion so it could tolerate slower growth rates, while higher temperatures would require faster growth rates. Considering that the optimized growth temperatures are usually a balance between maximizing smoothness and reducing defects (favoring higher T) and minimizing interdiffusion (favoring lower T), our current results indicate that growth rate should also be strongly considered in the materials optimization.

An interesting observation is the tendency for FGT to form abrupt interfaces even in the case for slow growth where the transition from Fe_3Ge_2 to FGT is relatively sharp (Figure 2a). While the role of Ge diffusion from the substrate is important for the formation of Fe_3Ge_2 as discussed above, the quick transition from Fe_3Ge_2 to FGT is possible because they are distinct thermodynamic phases. In more detail, for slow growth FGT, a Fe_3Ge_2 phase forms initially, where the excess Ge is provided by interdiffusion from the substrate (noting the Fe: Ge atomic flux ratio is 3:1). As the excess Ge drops below a certain value, the high Te flux causes the FGT phase to start forming at the surface. Now the system energetics favor the FGT phase more than Fe_3Ge_2 for subsequent growth, so the FGT phase quickly becomes dominant. This provides an explanation of how the interface between Fe_3Ge_2 and FGT could be relatively sharp instead of having a gradual transition for slow growth samples.

Identifying the significance of kinetically controlled growth for FGT is important for the future optimization of the material and its incorporation into epitaxial heterostructures. While the Fe_3Ge_2 phase might be specific to FGT on a Ge substrate, the issues of interdiffusion and chemical reaction with a substrate or underlayer are universally important for film growth. Our results suggest that the FGT growth rate may be used to control interdiffusion and chemical reaction with underlayers more generally, which will be useful for incorporating FGT into epitaxially grown vdW heterostructures.

CONCLUSION

In summary, we discovered that an important factor for optimizing FGT synthesis is the growth rate, which has an unexpected influence on thin film quality. The phenomenon is explained by energetics and kinetics of MBE growth where the stabilization of FGT is assisted by a higher deposition rate that inhibits the non-vdW Fe_3Ge_2 phase from forming. Atomic-scale imaging by STM and STEM confirm the structural quality of the surface and interface. The excellent magnetic properties with square out-of-plane hysteresis loops is confirmed by AHE, MCD, and spin-polarized STM measurements. Our results reveal an important way to think about and optimize MBE growth, leading to potentially better 2D materials.

AUTHOR INFORMATION

Corresponding Author

Roland K. Kawakami – *The Ohio State University, Department of Physics, Columbus, Ohio 43210, United States*; orcid.org/0000-0003-0245-9192;
Email: kawakami.15@osu.edu

Authors

Wenyi Zhou – *The Ohio State University, Department of Physics, Columbus, Ohio 43210, United States*
Alexander J. Bishop – *The Ohio State University, Department of Physics, Columbus, Ohio 43210, United States*
Menglin Zhu – *The Ohio State University, Department of Materials Science and Engineering, Columbus, Ohio 43210, United States*
Igor Lyalin – *The Ohio State University, Department of Physics, Columbus, Ohio 43210, United States*; orcid.org/0000-0001-8076-8914
Robert Walko – *The Ohio State University, Department of Physics, Columbus, Ohio 43210, United States*; orcid.org/0000-0002-8799-0531
Jay A. Gupta – *The Ohio State University, Department of Physics, Columbus, Ohio 43210, United States*
Jinwoo Hwang – *The Ohio State University, Department of Materials Science and Engineering, Columbus, Ohio 43210, United States*

Complete contact information is available at:
<https://pubs.acs.org/10.1021/acsaelm.2c00185>

Author Contributions

W.Z., A.J.B., and R.K.K. conceived the experiments. W.Z. and A.J.B. performed the MBE growth. M.Z. and J.H. performed the TEM measurements. A.J.B., R.W., and J.A.G. performed the STM measurements. I.L., W.Z., and R.K.K. performed the magnetotransport and magneto-optic measurements. All authors participated in data analysis and preparation of the manuscript.

Notes

The authors declare no competing financial interest.

ACKNOWLEDGMENTS

We thank Shuyu Cheng, Katherine Robinson, and Ryan Bailey-Crandell for technical assistance. This work was supported by AFOSR MURI 2D MAGIC Grant No. FA9550-19-1-0390 (MBE, magneto-optics), U.S. DOE Office of Science, Basic Energy Sciences Grant No. DE-SC0016379 (STM), and the Center for Emergent Materials, an NSF MRSEC, under Grant

No. DMR-2011876 (TEM, magnetotransport). Electron microscopy was performed at the Center for Electron Microscopy and Analysis (CEMAS) at The Ohio State University.

REFERENCES

- (1) Cenker, J.; Sivakumar, S.; Xie, K.; Miller, A.; Thijssen, P.; Liu, Z.; Dismukes, A.; Fonseca, J.; Anderson, E.; Zhu, X.; Roy, X.; Xiao, D.; Chu, J.-H.; Cao, T.; Xu, X. Reversible strain-induced magnetic phase transition in a van der Waals magnet. *Nat. Nanotechnol.* **2022**, *17*, 256–261.
- (2) Ni, Z.; Haglund, A. V.; Wang, H.; Xu, B.; Bernhard, C.; Mandrus, D. G.; Qian, X.; Mele, E. J.; Kane, C. L.; Wu, L. Imaging the Néel vector switching in the monolayer antiferromagnet MnPSe_3 with strain-controlled Ising order. *Nat. Nanotechnol.* **2021**, *16*, 782–787.
- (3) Wang, Y.; Wang, C.; Liang, S.-J.; Ma, Z.; Xu, K.; Liu, X.; Zhang, L.; Admasu, A. S.; Cheong, S.-W.; Wang, L.; Chen, M.; Liu, Z.; Cheng, B.; Ji, W.; Miao, F. Strain-Sensitive Magnetization Reversal of a van der Waals Magnet. *Adv. Mater.* **2020**, *32*, 2004533.
- (4) Jiang, S.; Li, L.; Wang, Z.; Mak, K. F.; Shan, J. Controlling magnetism in 2D CrI_3 by electrostatic doping. *Nat. Nanotechnol.* **2018**, *13*, 549–553.
- (5) Huang, B.; Clark, G.; Klein, D. R.; MacNeill, D.; Navarro-Moratalla, E.; Seyler, K. L.; Wilson, N.; McGuire, M. A.; Cobden, D. H.; Xiao, D.; Yao, W.; Jarillo-Herrero, P.; Xu, X. Electrical control of 2D magnetism in bilayer CrI_3 . *Nat. Nanotechnol.* **2018**, *13*, 544–548.
- (6) Song, T.; Cai, X.; Tu, M. W.-Y.; Zhang, X.; Huang, B.; Wilson, N. P.; Seyler, K. L.; Zhu, L.; Taniguchi, T.; Watanabe, K.; McGuire, M. A.; Cobden, D. H.; Xiao, D.; Yao, W.; Xu, X. Giant tunneling magnetoresistance in spin-filter van der Waals heterostructures. *Science* **2018**, *360*, 1214–1218.
- (7) Klein, D. R.; MacNeill, D.; Lado, J. L.; Soriano, D.; Navarro-Moratalla, E.; Watanabe, K.; Taniguchi, T.; Manni, S.; Canfield, P.; Fernández-Rossier, J.; Jarillo-Herrero, P. Probing magnetism in 2D van der Waals crystalline insulators via electron tunneling. *Science* **2018**, *360*, 1218–1222.
- (8) Wang, Z.; Sapkota, D.; Taniguchi, T.; Watanabe, K.; Mandrus, D.; Murguio, A. F. Tunneling Spin Valves Based on $\text{Fe}_3\text{GeTe}_2/\text{hBN}/\text{Fe}_3\text{GeTe}_2$ van der Waals Heterostructures. *Nano Lett.* **2018**, *18*, 4303–4308.
- (9) Zhong, D.; Seyler, K. L.; Linpeng, X.; Wilson, N. P.; Taniguchi, T.; Watanabe, K.; McGuire, M. A.; Fu, K.-M. C.; Xiao, D.; Yao, W.; Xu, X. Layer-resolved magnetic proximity effect in van der Waals heterostructures. *Nat. Nanotechnol.* **2020**, *15*, 187–191.
- (10) Fei, Z.; Huang, B.; Malinowski, P.; Wang, W.; Song, T.; Sanchez, J.; Yao, W.; Xiao, D.; Zhu, X.; May, A. F.; Wu, W.; Cobden, D. H.; Chu, J.-H.; Xu, X. Two-dimensional itinerant ferromagnetism in atomically thin Fe_3GeTe_2 . *Nat. Mater.* **2018**, *17*, 778–782.
- (11) Deng, Y.; Yu, Y.; Song, Y.; Zhang, J.; Wang, N. Z.; Sun, Z.; Yi, Y.; Wu, Y. Z.; Wu, S.; Zhu, J.; Wang, J.; Chen, X. H.; Zhang, Y. Gate-tunable room-temperature ferromagnetism in two-dimensional Fe_3GeTe_2 . *Nature* **2018**, *563*, 94–99.
- (12) Li, Q.; Yang, M.; Gong, C.; Chopdekar, R. V.; N'Diaye, A. T.; Turner, J.; Chen, G.; Scholl, A.; Shafer, P.; Arenholz, E.; Schmid, A. K.; Wang, S.; Liu, K.; Gao, N.; Admasu, A. S.; Cheong, S.-W.; Hwang, C.; Li, J.; Wang, F.; Zhang, X.; Qiu, Z. Patterning-Induced Ferromagnetism of Fe_3GeTe_2 van der Waals Materials beyond Room Temperature. *Nano Lett.* **2018**, *18*, 5974–5980.
- (13) Wang, H.; Liu, Y.; Wu, P.; Hou, W.; Jiang, Y.; Li, X.; Pandey, C.; Chen, D.; Yang, Q.; Wang, H.; Wei, D.; Lei, N.; Kang, W.; Wen, L.; Nie, T.; Zhao, W.; Wang, K. L. Above Room-Temperature Ferromagnetism in Wafer-Scale Two-Dimensional van der Waals Fe_3GeTe_2 Tailored by a Topological Insulator. *ACS Nano* **2020**, *14*, 10045–10053.
- (14) Alghamdi, M.; Lohmann, M.; Li, J.; Jothi, P. R.; Shao, Q.; Aldosary, M.; Su, T.; Fokwa, B. P. T.; Shi, J. Highly Efficient Spin–Orbit Torque and Switching of Layered Ferromagnet Fe_3GeTe_2 . *Nano Lett.* **2019**, *19*, 4400–4405.
- (15) Kao, I.-H.; Muzzio, R.; Zhang, H.; Zhu, M.; Gobbo, J.; Weber, D.; Rao, R.; Li, J.; Edgar, J. H.; Goldberger, J. E.; Yan, J.; Mandrus, D. G.; Hwang, J.; Cheng, R.; Katoch, J.; Singh, S. Field-free deterministic switching of a perpendicularly polarized magnet using unconventional spin-orbit torques in WTe_2 . *arXiv* **2020**, No. 2012.12388, DOI: 10.48550/arXiv.2012.12388.
- (16) Wang, X.; Tang, J.; Xia, X.; He, C.; Zhang, J.; Liu, Y.; Wan, C.; Fang, C.; Guo, C.; Yang, W.; Guang, Y.; Zhang, X.; Xu, H.; Wei, J.; Liao, M.; Lu, X.; Feng, J.; Li, X.; Peng, Y.; Wei, H.; Yang, R.; Shi, D.; Zhang, X.; Han, Z.; Zhang, Z.; Zhang, G.; Yu, G.; Han, X. Current-driven magnetization switching in a van der Waals ferromagnet Fe_3GeTe_2 . *Science Advances* **2019**, *5*, No. eaaw8904.
- (17) Wang, H.; Wu, H.; Liu, Y.; Chen, D.; Pandey, C.; Yin, J.; Wei, D.; Lei, N.; Zhang, J.; Lu, H.; Shi, S.; Li, P.; Fert, A.; Wang, K. L.; Nie, T.; Zhao, W. Room temperature energy-efficient spin-orbit torque switching in wafer-scale all-vdW heterostructure. *arXiv* **2021**, 2111.14128 DOI: 10.48550/arXiv.2111.14128.
- (18) Wu, Y.; Zhang, S.; Zhang, J.; Wang, W.; Zhu, Y. L.; Hu, J.; Yin, G.; Wong, K.; Fang, C.; Wan, C.; Han, X.; Shao, Q.; Taniguchi, T.; Watanabe, K.; Zang, J.; Mao, Z.; Zhang, X.; Wang, K. L. Néel-type skyrmion in $\text{WTe}_2/\text{Fe}_3\text{GeTe}_2$ van der Waals heterostructure. *Nat. Commun.* **2020**, *11*, 3860.
- (19) Yang, M.; Li, Q.; Chopdekar, R. V.; Dhall, R.; Turner, J.; Carlström, J. D.; Ophus, C.; Klewe, C.; Shafer, P.; N'Diaye, A. T.; Choi, J. W.; Chen, G.; Wu, Y. Z.; Hwang, C.; Wang, F.; Qiu, Z. Q. Creation of skyrmions in van der Waals ferromagnet Fe_3GeTe_2 on $(\text{Co/Pd})_n$ superlattice. *Science Advances* **2020**, *6*, No. eabb5157.
- (20) Park, T.-E.; Peng, L.; Liang, J.; Hallal, A.; Yasin, F. S.; Zhang, X.; Song, K. M.; Kim, S. J.; Kim, K.; Weigand, M.; Schütz, G.; Finizio, S.; Raabe, J.; Garcia, K.; Xia, J.; Zhou, Y.; Ezawa, M.; Liu, X.; Chang, J.; Koo, H. C.; Kim, Y. D.; Chshiev, M.; Fert, A.; Yang, H.; Yu, X.; Woo, S. Néel-type skyrmions and their current-induced motion in van der Waals ferromagnet-based heterostructures. *Phys. Rev. B* **2021**, *103*, 104410.
- (21) Zhu, T.; Bishop, A. J.; Zhou, T.; Zhu, M.; O'Hara, D. J.; Baker, A. A.; Cheng, S.; Walko, R. C.; Repicky, J. J.; Liu, T.; Gupta, J. A.; Jozwiak, C. M.; Rotenberg, E.; Hwang, J.; Zutic, I.; Kawakami, R. K. Synthesis, Magnetic Properties, and Electronic Structure of Magnetic Topological Insulator MnBi_2Se_4 . *Nano Lett.* **2021**, *21*, 5083–5090.
- (22) Liu, S.; Yuan, X.; Zou, Y.; Sheng, Y.; Huang, C.; Zhang, E.; Ling, J.; Liu, Y.; Wang, W.; Zhang, C.; Zou, J.; Wang, K.; Xiu, F. Wafer-scale two-dimensional ferromagnetic Fe_3GeTe_2 thin films grown by molecular beam epitaxy. *npj 2D Materials and Applications* **2017**, *1*, 37.
- (23) Roemer, R.; Liu, C.; Zou, K. Robust ferromagnetism in wafer-scale monolayer and multilayer Fe_3GeTe_2 . *npj 2D Materials and Applications* **2020**, *4*, 33.
- (24) Chen, X.; Wang, H.; Liu, H.; Wang, C.; Wei, G.; Fang, C.; Wang, H.; Geng, C.; Liu, S.; Li, P.; Yu, H.; Zhao, W.; Miao, J.; Li, Y.; Wang, L.; Nie, T.; Zhao, J.; Wu, X. Generation and Control of Terahertz Spin Currents in Topology-Induced 2D Ferromagnetic $\text{Fe}_3\text{GeTe}_2/\text{Bi}_2\text{Te}_3$ Heterostructures. *Advanced Materials* **2022**, *34*, 2106172.
- (25) Ribeiro, M.; Gentile, G.; Marty, A.; Dosenovic, D.; Okuno, H.; Vergnaud, C.; Jacquot, J.-F.; Jalabert, D.; Longo, D.; Ohresser, P.; Hallal, A.; Chshiev, M.; Boule, O.; Bonell, F.; Jamet, M. Large-scale epitaxy of two-dimensional van der Waals room-temperature ferromagnet Fe_3GeTe_2 . *arXiv* **2021**, No. 2106.12808, DOI: 10.48550/arXiv.2106.12808.
- (26) Schlom, D. G.; Haeni, J. H.; Lettieri, J.; Theis, C. D.; Tian, W.; Jiang, J. C.; Pan, X. Q. Oxide nano-engineering using MBE. *Materials Science and Engineering: B* **2001**, *87*, 282–291.
- (27) Theis, C. D.; Yeh, J.; Schlom, D. G.; Hawley, M. E.; Brown, G. W.; Jiang, J. C.; Pan, X. Q. Adsorption-controlled growth of $\text{Bi}_4\text{Ti}_3\text{O}_{12}$ by reactive MBE. *Appl. Phys. Lett.* **1998**, *72*, 2817–2819.
- (28) Vaughn, D. D.; Sun, D.; Moyer, J. A.; Biacchi, A. J.; Misra, R.; Schiffer, P.; Schaak, R. E. Solution-Phase Synthesis and Magnetic Properties of Single-Crystal Iron Germanide Nanostructures. *Chem. Mater.* **2013**, *25*, 4396–4401.

(29) Goswami, R.; Kioseoglou, G.; Hanbicki, A. T.; van't Erve, O. M. J.; Jonker, B. T.; Spanos, G. Growth of ferromagnetic nanoparticles in Ge:Fe thin films. *Appl. Phys. Lett.* **2005**, *86*, 032509.

(30) Deiseroth, H.-J.; Aleksandrov, K.; Reiner, C.; Kienle, L.; Kremer, R. K. Fe_3GeTe_2 and Ni_3GeTe_2 – Two New Layered Transition-Metal Compounds: Crystal Structures, HRTEM Investigations, and Magnetic and Electrical Properties. *Eur. J. Inorg. Chem.* **2006**, *2006*, 1561–1567.

(31) Yi, J.; Zhuang, H.; Zou, Q.; Wu, Z.; Cao, G.; Tang, S.; Calder, S. A.; Kent, P. R. C.; Mandrus, D.; Gai, Z. Competing antiferromagnetism in a quasi-2D itinerant ferromagnet: Fe_3GeTe_2 . *2D Materials* **2017**, *4*, 011005.

(32) Chen, B.; Yang, J.; Wang, H.; Imai, M.; Ohta, H.; Michioka, C.; Yoshimura, K.; Fang, M. Magnetic Properties of Layered Itinerant Electron Ferromagnet Fe_3GeTe_2 . *J. Phys. Soc. Jpn.* **2013**, *82*, 124711.

(33) Repicky, J.; Wu, P.-K.; Liu, T.; Corbett, J. P.; Zhu, T.; Cheng, S.; Ahmed, A. S.; Takeuchi, N.; Guerrero-Sanchez, J.; Randeria, M.; Kawakami, R. K.; Gupta, J. A. Atomic-scale visualization of topological spin textures in the chiral magnet MnGe. *Science* **2021**, *374*, 1484–1487.

Recommended by ACS

Electric-Field-Induced Room-Temperature Antiferroelectric–Ferroelectric Phase Transition in van der Waals Layered GeSe

Zhao Guan, Chungang Duan, *et al.*

JANUARY 03, 2022
ACS NANO

READ 

Structure-Driven, Ferroelectric Wake-Up Effect for Electrical Fatigue Relief

Teng Lu, Yun Liu, *et al.*

JULY 29, 2020
CHEMISTRY OF MATERIALS

READ 

Chemical Composition Control at the Substrate Interface as the Key for FeSe Thin-Film Growth

Yukiko Obata, Silvia Haindl, *et al.*

OCTOBER 26, 2021
ACS APPLIED MATERIALS & INTERFACES

READ 

Antiphase-Boundary-Engineered Domain Switching in a (110)-Oriented BiFeO₃ Film

Yangyang Zhang, Yimei Zhu, *et al.*

JULY 15, 2021
ACS APPLIED ELECTRONIC MATERIALS

READ 

Get More Suggestions >